

# Searching for an interstellar medium association for HESS J1534–571

Nigel I. Maxted<sup>1,2\*</sup>, C. Braiding,<sup>1</sup> G. F. Wong,<sup>1,2</sup> G. P. Rowell,<sup>3</sup> M. G. Burton,<sup>1,4</sup> M. D. Filipović,<sup>2</sup> F. Voisin,<sup>3</sup> D. Urošević,<sup>5,6</sup> B. Vukotić,<sup>7</sup> M. Z. Pavlović,<sup>5</sup> H. Sano<sup>8</sup> and Y. Fukui<sup>8</sup>

<sup>1</sup>*School of Physics, The University of New South Wales, Sydney, 2052, Australia*

<sup>2</sup>*Western Sydney University, Locked Bag 1797, Penrith, NSW 2751, Australia*

<sup>3</sup>*School of Physical Sciences, The University of Adelaide, Adelaide, 5005, Australia*

<sup>4</sup>*Armagh Observatory and Planetarium, College Hill, Armagh, BT61 9DG, Northern Ireland, United Kingdom*

<sup>5</sup>*Department of Astronomy Faculty of Mathematics, University of Belgrade Studentski trg 16, 11000 Belgrade, Serbia*

<sup>6</sup>*Isaac Newton Institute of Chile Yugoslavia Branch, Serbia*

<sup>7</sup>*Astronomical Observatory, Volgina 7, P.O.Box 74 11060 Belgrade, Serbia*

<sup>8</sup>*Department of Physics, Nagoya University, Furo-cho, Chikusa-ku, Nagoya 464-8601, Japan*

Accepted 2018 July 03. Received 2018 July 01; in original form 2018 April 27

## ABSTRACT

The Galactic supernova remnant HESS J1534–571 (also known as G323.7–1.0) has a shell-like morphology in TeV gamma-ray emission and is a key object in the study of cosmic ray origin. Little is known about its distance and local environment. We examine Mopra <sup>12</sup>CO/<sup>13</sup>CO(1-0) data, Australian Telescope Compact Array HI, and Parkes HI data towards HESS J1534–571. We trace molecular clouds in at least five velocity ranges, including clumpy interstellar medium structures near a dip in HI emission at a kinematic velocity consistent with the Scutum-Crux arm at ~3.5 kpc. This feature may be a cavity blown-out by the progenitor star, a scenario that suggests HESS J1534–571 resulted from a core-collapse event. By employing parametrisations fitted to a sample of supernova remnants of known distance, we find that the radio continuum brightness of HESS J1534–571 is consistent with the ~3.5 kpc kinematic distance of the Scutum-Crux arm HI dip. Modelling of the supernova evolution suggests an ~8–24 kyr age for HESS J1534–571 at this distance.

**Key words:** ISM: cosmic rays – ISM: supernova remnants – gamma-rays: ISM – ISM: molecules

## 1 INTRODUCTION

The Galactic supernova remnant candidate G323.7–1.0 was initially discovered in 843 MHz radio continuum emission (see Green et al. 2014). Its nature as a shell-type supernova remnant (SNR) was confirmed with the significant detection of a corresponding TeV gamma-ray shell, HESS J1534–571, as shown in Figure 1 (Abdalla et al. 2018). Supernova remnants with associated gamma-ray emission are key targets in the search for Galactic sources of cosmic ray hadrons (hereafter CRs). Supernova shocks with velocities  $>1000 \text{ km s}^{-1}$  may be able to host the diffusive shock acceleration process for particle acceleration (e.g. Bell 1978), which would help to explain the observed flux of Galactic CRs up to energies of several PeV.

Some mature ( $\sim 10^4 \text{ yr}$ ) shell-type SNRs have been proven to be CR accelerators (e.g. IC 443 and W44, Ackermann et al. 2013) through observations of high energy spectra which have so-called ‘pion-bumps’ - signatures of neutral-pion creation and decay resulting from CR interactions with gas (i.e. a proton-proton mechanism). Some SNRs have a spatial correspondence between gas and gamma-rays that strongly suggests this mechanism (e.g. W28 and W49, Aharonian et al. 2008; Abdalla et al. 2016). In these cases, it is believed that the SNR shocks have created the conditions needed to accelerate protons to TeV energies. These protons (TeV-energy CR hadrons) have then diffused into nearby molecular clouds where proton-proton interactions lead to observable gamma-ray emission that reflects the morphology of the associated gas. Corresponding populations of high-energy electrons, also accelerated by the SNR shocks, have cooled to sub-TeV energies more quickly than protons

\* Email: n.maxted@unsw.edu.au

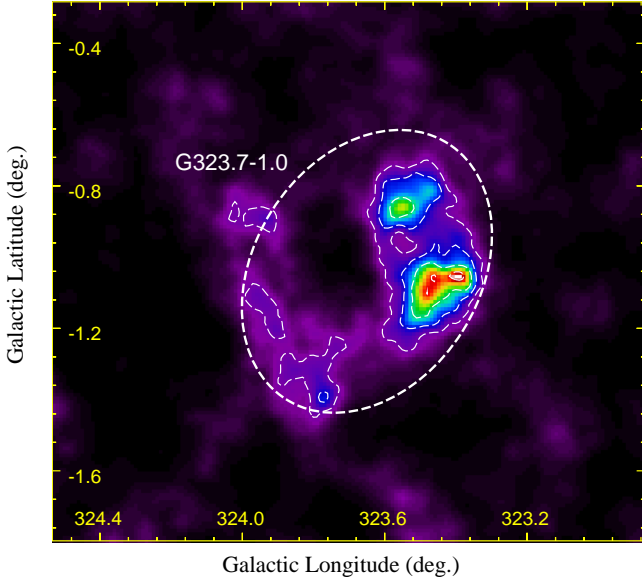


**Figure 1.** High Energy Stereoscopic System (HESS)  $\sim 0.6$ – $100$  TeV gamma-ray significance image of HESS J1534–571 (Abdalla et al. 2018). Corresponding  $3$ ,  $4$ ,  $5$  and  $6\sigma$  TeV gamma-ray emission contours are overlaid. A white-dashed ellipse indicates the position of SNR G323.7–1.0 (Green et al. 2014), which was first identified in 843 MHz radio continuum emission from the Molonglo Observatory Synthesis telescope (MOST) survey. The ellipse has a centre of  $[\alpha, \delta, J2000]=[05:34:30.1-57:12:03]$  and axes diameter of  $51' \times 38'$ .

in this scenario due to the synchrotron emission mechanism. The growing list of SNRs with strong ties to TeV CRs tells a convincing story about the role of these objects in CR acceleration at TeV energies.

A sub-class of gamma-ray SNRs with shell-type morphology at TeV energies is comprised by eight objects - RX J1713.7–3946, HESS J1731–347, RX J0852.0–4622, RCW 86, SN 1006 and three new SNRs and SNR candidates, HESS J1614–518, HESS J1912+101 and HESS J1534–571. The former 5 of this group (generally aged  $\sim 10^3$  yr), have a GeV–TeV spectral shape that appears to favour a gamma-ray production process that involves high-energy electrons (e.g. Acero et al. 2015) - inverse-Compton scattering of low-energy photons (leptonic emission), within or near the SNR shock. However, it has been argued that a clumpy interstellar medium might be able to alter the expected hadronic gamma-ray spectral shape of young TeV SNRs if energy-dependent diffusion into dense gas clumps within or near the SNR shock front plays a significant role (Gabici et al. 2009; Zirakashvili & Aharonian 2010; Inoue et al. 2012; Fukui et al. 2012; Maxted et al. 2012; Gabici & Aharonian 2014). Evidence of a gamma-ray production mechanism inherently linked to gas density is present in the strong correspondence between gas proton density and gamma-ray flux in RX J1713.7–3946, HESS J1731–347 and RX J0852.0–4622 (Fukui et al. 2012; Fukuda et al. 2014; Fukui et al. 2017, respectively). The authors point to the hadronic gamma-ray production mechanism as the likely explanation. In this respect, knowledge of the ISM local to SNRs is important for understanding the nature of the gamma-ray production in individual cases.

Gas associations for young ( $\sim 10^3$  yr) shell-type SNRs have been difficult to prove definitively. Older ( $\sim 10^4$  yr) SNRs may exhibit signatures of shocked gas that have corresponding measurable kinematic distances, e.g. observations of spectral line broadening or shock-tracing SiO or 1720 MHz OH emission (e.g. Nicholas et al. 2012; Frail et al. 1996, respectively). In contrast, the high-speed shocks ( $>1000$  km s $^{-1}$ ) of young Galactic shell-type SNRs have not yet begun to exhibit clear markers of shocked gas that contain line of sight velocity information. In such cases, gas associations are sometimes inferred using morphological correspondence between X-rays and gamma-rays, and H I and CO. This is the case for SNRs RX J1713.7–3946, HESS J1731–347 and RX J0852.0–4622 (Fukui et al. 2012; Fukuda et al. 2014; Fukui et al. 2017).

HESS J1534–571 may share some similarities with RX J1713.7–3946, HESS J1731–347 and RX J0852.0–4622, both morphologically and spectrally. Araya (2017) recently argued for a leptonic scenario in HESS J1534–571, following a GeV gamma-ray spectral analysis. In this scenario, a distance of  $\sim 4$ – $5$  kpc was inferred by the level of far infrared emission required to produce the observed gamma-ray emission via an assumed Inverse-Compton scattering scenario. Although initial attempts to find a SNR-association in Suzaku X-ray data revealed no significant counterpart (Puehlhofer et al. 2016; Abdalla et al. 2018), regions of soft 0.5–3 keV X-rays towards HESS J1534–571 were later discovered, while 6.4 keV Fe-line emission suggested the existence of an ionising population of  $\sim 10$  MeV-energy CR protons (Saji et al. 2018). Soft X-ray absorption modelling suggested a SNR at distance of  $\sim 6 \pm 2$  kpc (Saji et al. 2018), in agreement with the Araya distance ( $\sim 4$ – $5$  kpc, assuming leptonic gamma-ray emission). A specific gas association at such distances has not been identified, however one is suggested in our study.

The local environment of individual SNRs (among other parameters) can also have an effect on the robustness of the radio surface brightness to diameter relation (e.g. Kostić et al. 2016), i.e.  $\Sigma$ – $D$  relation, particularly in the case of shock-cloud interactions (see Pavlović et al. 2018, for detailed modelling). In the case of HESS J1534–571, which is suggested to be under-luminous at radio wavelengths, Abdalla et al. (2018) scaled the  $\Sigma$ – $D$  relation to match the case of the shell-type SNR RX J1713.7–3946, which is also known to be radio-dim. The resultant inferred distance was  $\sim 5$  kpc, consistent with aforementioned values ( $6 \pm 2$  and  $\sim 4$ – $5$  kpc Araya 2017; Saji et al. 2018). This may imply some similarities between RX J1713.7–3946 and HESS J1534–571, and the ISM local to both. RX J1713.7–3946 exists in a particularly clumpy medium, but the environment local to HESS J1534–571 has not been examined at a sufficient angular resolution until now.

The identification of a gas association for HESS J1534–571 will help to further constrain the distance and pinpoint potential CR target material related to gamma-ray emission. For this purpose, Mopra CO(1–0) data and SGPS H I data are employed to investigate the ISM towards this new shell-type gamma-ray SNR. We particularly target molecular clumps.

We outline the characteristics of our data and analysis in Section 2. We present new Mopra maps of CO(1–0) emission towards HESS J1534–571 in Section 3. In Section 4 we

identify molecular clump features consistent with an association with HESS J1534–571 before discussing some implications for the implied distance. The association is reinforced by a statistical study of the radio flux of HESS J1534–571 compared to a sample of SNRs.

## 2 OBSERVATIONS

In this study, we utilise Mopra CO Galactic Plane Survey data to identify molecular clumps in the line of sight of the Galactic SNR HESS J1534–571. Mopra spectral CO(1-0) data has a superior angular resolution to previously-published gas data towards the HESS J1534–571 region. Public Southern Galactic Plane Survey (SGPS) H I data is re-examined (following studies by Abdalla et al. 2018) in support of this new Mopra data-set. Where relevant to interpreting multi-wavelength data, molecular column densities and masses are calculated.

### 2.1 The Mopra CO Galactic Plane Survey at 3 mm

Spectral data of the J=1-0 transition of CO isotopologues was taken as part of the Mopra Galactic Plane CO Survey<sup>1</sup> (see Burton et al. 2013)<sup>2</sup>. The <sup>12</sup>CO<sup>3</sup>, <sup>13</sup>CO, C<sup>18</sup>O and C<sup>17</sup>O(1-0) were targeted in the Mopra survey, but only the former two of these isotopologues are exploited in this paper, as they are the brightest emitters.

Details of the latest Mopra CO data processing procedures are presented in Braiding et al. (2015) and Braiding et al. (2018). Data towards the HESS J1534–571 field have a velocity coverage of  $-596 \text{ km s}^{-1} < v_{LSR} < +501 \text{ km s}^{-1}$  and  $-524 \text{ km s}^{-1} < v_{LSR} < +247 \text{ km s}^{-1}$  for CO(1-0) and <sup>13</sup>CO(1-0), respectively. The angular resolution and velocity resolution are  $35''$  and  $0.1 \text{ km s}^{-1}$ , respectively, across eight 4096-channel dual-polarisation bands. The extended beam efficiency used to recalibrate the antenna temperature of Mopra at 115 GHz is 0.55 (Ladd et al. 2005).

### 2.2 21 cm SGPS HI data

Publicly-available 21 cm H I data from the SGPS (see McClure-Griffiths et al. 2005, for details) was examined in support of our CO analysis (see Appendix A). H I fits cubes were created by combining Parkes single-dish and Australia Telescope Compact Array (ATCA) interferometer data to cover both large and small-scale structures of atomic gas with a resultant angular and velocity resolution of  $\sim 2'$  and  $\sim 0.8 \text{ km s}^{-1}$ , respectively. H I data cubes have been calibrated to remove radio-continuum sources.

### 2.3 Spectral line examination

We examine Mopra CO and <sup>13</sup>CO(1-0) emission to identify molecular cloud components that might be candidates for association with HESS J1534–571. Mopra CO(1-0) and

<sup>13</sup>CO(1-0) integrated intensity images are shown in Figures 2 and 3. Velocity-integration ranges were chosen to highlight individual spectral features identified in the CO(1-0) cube. MIRIAD software was used for this task (Sault et al. 1995).

Figure 4 and 5a, b and c display the velocity structure of the CO(1-0), <sup>13</sup>CO(1-0) and H I emission, respectively. Galactic arm structures are discernible (discussed in Section 3) and consistent with that of the Columbia CO survey (Dame et al. 2001), which is also shown in Figure 4. Figure 5d is used as a guide for the conversion between kinematic velocity and kinematic distance.

## 2.4 Parameter calculations

### 2.4.1 <sup>12</sup>CO Analysis

Column densities and masses were calculated for CO cores identified in this analysis. An X-factor was used to convert CO(1-0) emission into H<sub>2</sub> column density,  $N = X \int I_\nu d\nu$  [ $\text{cm}^{-2}(\text{K km s}^{-1})^{-1}$ ], where  $I_\nu d\nu$  is the velocity-integrated emission,  $X$  is the X-factor and  $N$  is the molecular column density (e.g. Lang 1980). In our analysis, we use a range of CO X-factors,  $1.3 \times 10^{20} \text{ cm}^{-2} (\text{K km s}^{-1})^{-1}$  to account for the observed scatter of this value (e.g. Bolatto et al. 2013; Okamoto et al. 2017).

### 2.4.2 <sup>13</sup>CO Analysis

Where the less-abundant <sup>13</sup>CO(1-0) transition is present, we calculate the CO optical depth to account for the attenuation in CO(1-0) via the prescription in Wilson et al. (2013). With the assumption that <sup>13</sup>CO and <sup>12</sup>CO emission are emitted from the same uniform excitation temperature region, we create excitation temperature maps via

$$T = \frac{5.5}{\ln \left( 1 + \frac{5.5}{T_B^{12} + 0.82} \right)} \quad [\text{K}] \quad (1)$$

which is then used to calculate the <sup>13</sup>CO(1-0) optical depth,

$$\tau_0^{13} = -\ln \left[ 1 - \frac{T_B^{13}}{5.3} \left[ \left( \exp \left[ \frac{5.3}{T} \right] - 1 \right)^{-1} - 0.16 \right]^{-1} \right] \quad (2)$$

where  $T_B^{12}$  and  $T_B^{13}$  are the <sup>12</sup>CO and <sup>13</sup>CO brightness temperatures, respectively. Equation 2 is valid under the assumption that the <sup>12</sup>CO(1-0) optical depth is large compared to unity and the <sup>13</sup>CO(1-0) optical depth is small compared to unity. The <sup>13</sup>CO column density was then calculated by

$$N(\text{total})_{\text{CO}}^{13} = 3.0 \times 10^{14} \frac{T \int \tau^{13}(\nu) d\nu}{1 - \exp(-5.3/T)} \quad (3)$$

We used an assumed <sup>13</sup>CO abundance to create a H<sub>2</sub> column density map. Commonly, the H<sub>2</sub> abundance relative to <sup>13</sup>CO is quoted to be  $3.6 \times 10^5$  (Frerking et al. 1982; Bachiller & Cernicharo 1986; Cernicharo & Bachiller 1984). We assume a 50% systematic error in this value, similar to the observed variation in <sup>12</sup>CO abundance, and derive a range of masses based on a <sup>13</sup>CO abundance of 1.4 to  $4.2 \times 10^{-6}$  relative to H<sub>2</sub>.

<sup>1</sup> <http://phys.unsw.edu.au/mopraco/>

<sup>2</sup> see [www.mopra.org/data/](http://www.mopra.org/data/)

<sup>3</sup> hereafter CO

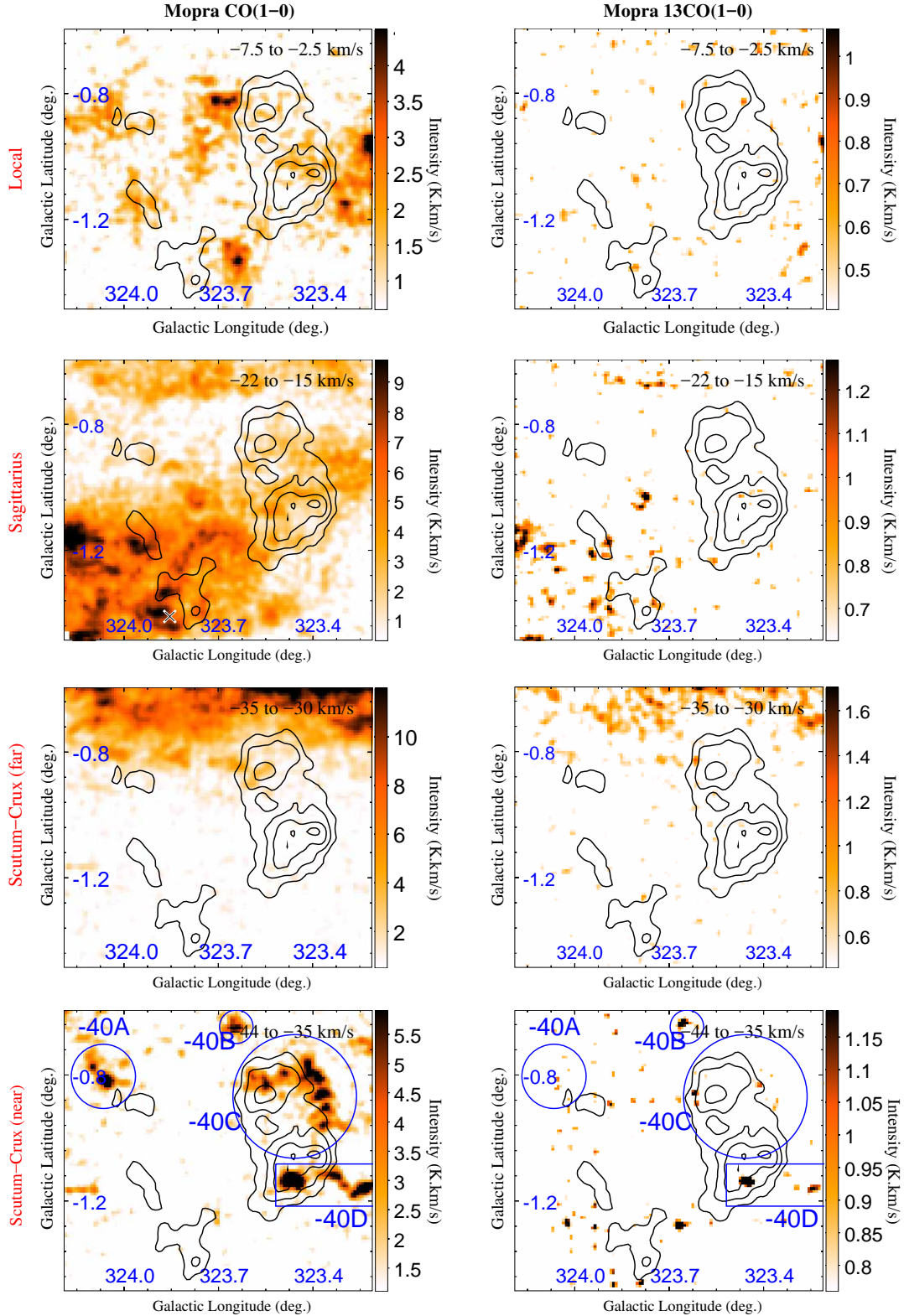


**Figure 2.** Velocity integrated CO(1-0) (left) and  $^{13}\text{CO}(1-0)$  (right) images. Integration ranges which are indicated inset on each image, are  $-7.5$  to  $-2.5$ ,  $-22$  to  $-15$ ,  $-35$  to  $-30$  and  $-44$  to  $-35$   $\text{km s}^{-1}$ , from top to bottom, respectively. HESS 3, 4, 5 and  $6\sigma > 1$  TeV gamma-ray significance contours (thick black) are overlaid (Abdalla et al. 2018). Suggested Galactic arm associations are indicated in red on along the left side of the figure for each row. In the bottom images, circular regions corresponding to parameter calculations in Table 1 are indicated.



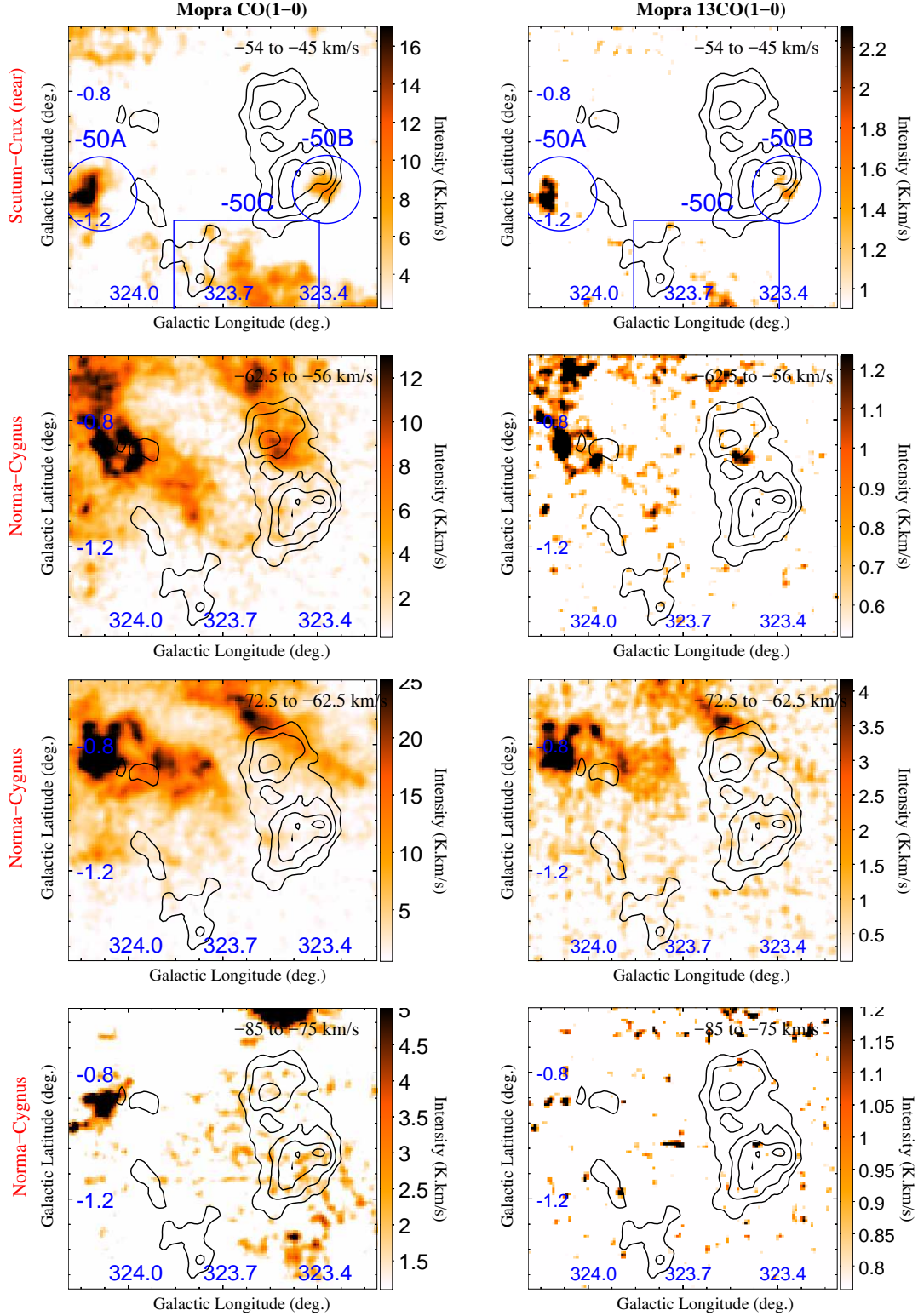


**Figure 3.** Velocity integrated CO(1-0) (left) and  $^{13}\text{CO}(1-0)$  (right) images. Integration ranges which are indicated inset on each image, are  $-55.4$  to  $-45$ ,  $-62.5$  to  $-56$ ,  $-72.5$  to  $-62.5$  and  $-85$  to  $-75$   $\text{km s}^{-1}$ , from top to bottom, respectively. HESS 3, 4, 5 and  $6\sigma > 1$  TeV gamma-ray significance contours (thick black) are overlaid (Abdalla et al. 2018). Suggested Galactic arm associations are indicated in red on along the left side of the figure for each row. In the top images, circular regions corresponding to parameter calculations in Table 1 are indicated.

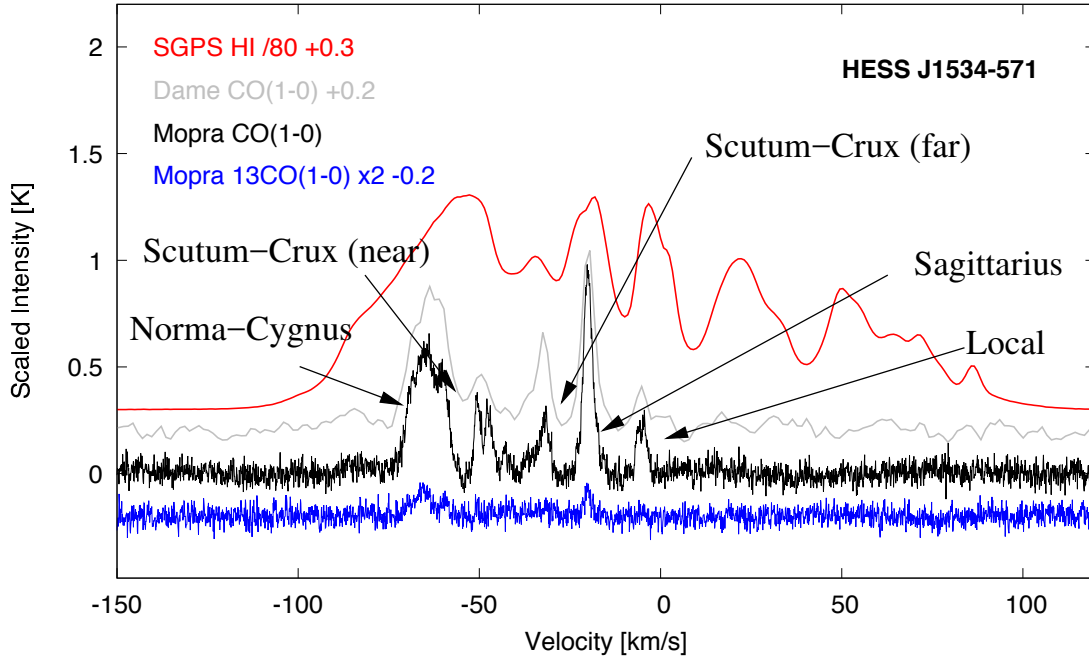


**Figure 4.** Mopra CO, Mopra  $^{13}\text{CO}$  and SGPS HI emission towards the elliptical MOST 843 MHz emission region encompassing HESS J1534–571, as displayed in Figure 1.

### 2.4.3 Mass Calculation

$\text{H}_2$  column density maps were converted to maps of mass/pixel by  $M_{\text{H}_2} = 2m_{\text{H}}A_{\text{pix}}N_{\text{H}_2}$ , where  $m_{\text{H}}$  is the mass of a H atom,  $A_{\text{pix}}$  is the area of a fits file pixel and  $N_{\text{H}_2}$  is the average  $\text{H}_2$  column density within a given region. The mass of a region could then be simply calculated by summing the corresponding pixels. This method is applied for both  $^{12}\text{CO}$  and  $^{13}\text{CO}$ -derived column densities. Due to sensitivity limitations, the  $^{13}\text{CO}$ -derived mass includes contributions from fewer map pixels than the  $^{12}\text{CO}$ -derived mass in all cases. Where clear  $^{13}\text{CO}$  emission is not present, mass calculations are not derived from  $^{13}\text{CO}$  images.

## 3 RESULTS

Figures 2 and 3 display CO(1-0) components identified in this study, alongside  $^{13}\text{CO}$ (1-0) emission maps of corresponding velocity ranges. In the following sections, arranged by likely Galactic Arm Association (with reference to Figure 4 and 5). Along the left side of Figures 2 and 3 are labels of Galactic arms corresponding to the headings of Sections 3.1 to 3.5, which describe the features seen CO/ $^{13}\text{CO}$ (1-0) maps. For some clumpy structures present in maps which are argued to be a candidates for association with HESS J1534–571 (see Section 4.1), we display spectral line parameters and derived physical parameters in Table 1.

### 3.1 Local gas

In Figure 2, CO(1-0) emission between  $-7.5$  and  $-2.5\text{ km s}^{-1}$  is at a velocity consistent with local gas. Molecular gas clumps exist at the north and south of boundary of HESS J1534–571, and outside the western boundary. With

the exception of the western map boundary, minimal  $^{13}\text{CO}$  emission is seen.

### 3.2 The Sagittarius Arm

CO(1-0)-traced molecular gas between  $-22$  and  $-15\text{ km s}^{-1}$  is likely associated with the Sagittarius Arm at a distance of  $\sim 1.2\text{ kpc}$ . This gas is extended with diffuse components coincident with much of HESS J1534–571, and has a total mass of  $1.7\text{--}5.0\text{ M}_{\odot}$  within the radio continuum boundary (shown in Figure 1). Some  $^{13}\text{CO}$  emission is towards the south-east of the region.

### 3.3 The Scutum-Crux Arm (far)

CO(1-0)-traced molecular gas between  $-35$  and  $-30\text{ km s}^{-1}$  is likely associated with the far-side of the Scutum-Crux Arm at a distance of  $\sim 12\text{ kpc}$ . The gas, which contains dense  $^{13}\text{CO}$ -traced clumps, is only observed towards the inner plane, to the north of HESS J1534–571.

### 3.4 The Scutum-Crux Arm (near)

CO(1-0)-traced molecular gas between  $-54$  and  $-35\text{ km s}^{-1}$  is likely associated with the near-side of the Scutum-Crux Arm at a distance of  $\sim 3.5\text{ kpc}$ . Two velocity slices of this arm are displayed in Figure 2 (bottom) and 3 (top).

Between  $-44$  and  $-35\text{ km s}^{-1}$ , a series of approximately twelve 1 to 3 arcminute CO(1-0)-traced clumps are present. These components are separated into regions labelled –40A, B, C and D in Figure 2. Corresponding masses are on the order of  $10^2$  to  $10^3\text{ M}_{\odot}$  (see Table 1), with most of the mass being either coincident or directly adjacent to the brightest gamma-ray component in the west. In Region –40C the

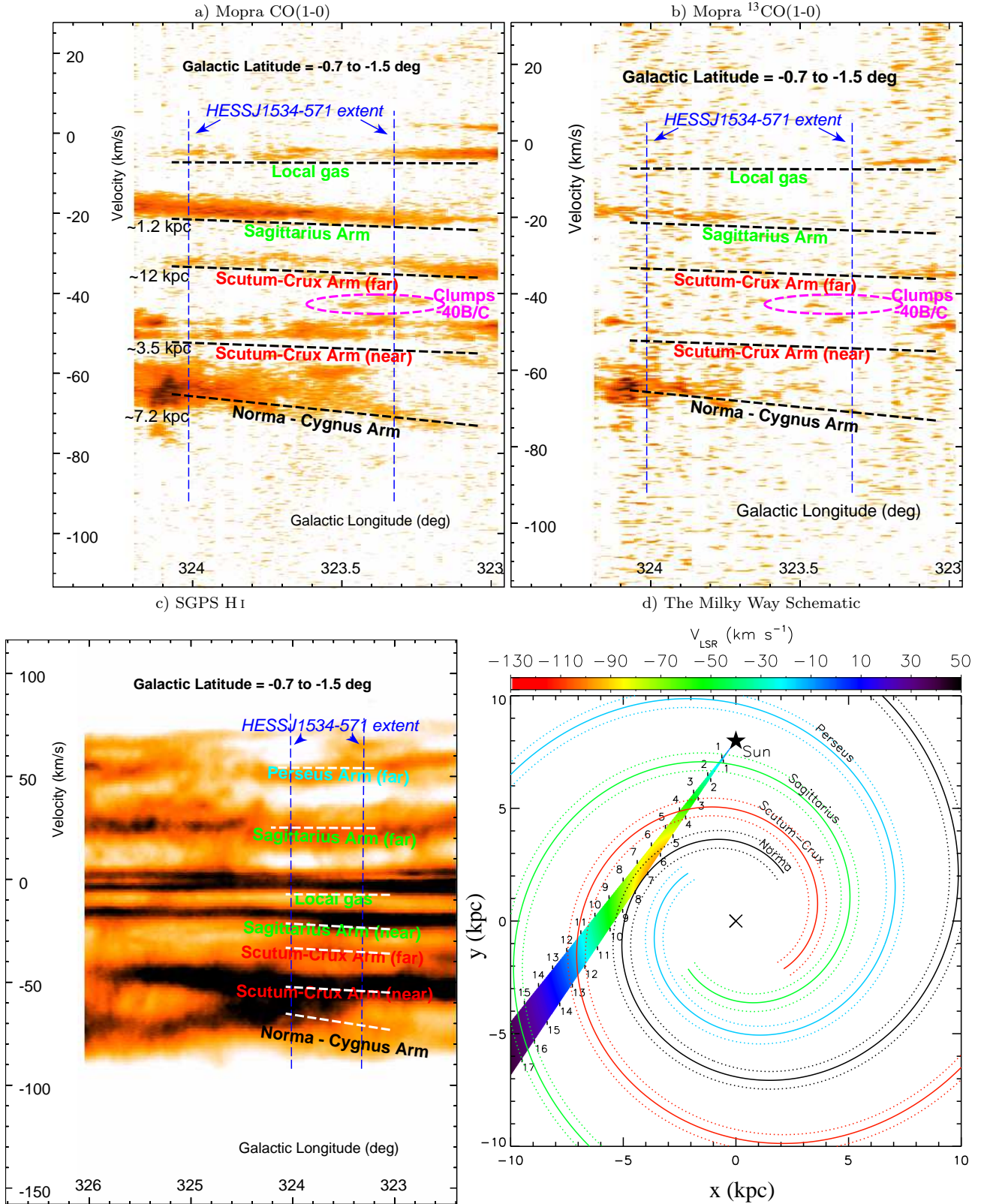


**Figure 5.** Plots of Mopra CO(1-0) (a, top-left), Mopra  $^{13}\text{CO}(1-0)$  (b, top-right) and SGPS H I (c, bottom) emission as a function of line of sight velocity and Galactic Longitude. CO,  $^{13}\text{CO}$  and H I emission has been spatially integrated between  $-1.5$  and  $-0.7^\circ$ . In images a, b and c, blue dotted lines indicate the longitudinal extent of HESS J1534–571, and plausible Galactic arm associations are stated (see d). These lines correspond to the same coordinates in each image. Clumps –40B/C are indicated by ovals in figures a and b. d) A diagram of the Galactic rotation model of the Milky Way Galaxy (see Vallée 2016, for details). Based on (d), distances to corresponding arm features are shown in (a).



**Table 1.** Spectral line parameters and derived physical parameters for selected clump features. Velocity of peak ( $v_{\text{LSR}}$ ), line full-width half-maximum ( $\Delta v_{\text{FWHM}}$ ), peak  $\text{H}_2$  column density calculated via two methods (X-factor method,  $N_{\text{H}_2}^{12}$ , and the  $^{13}\text{CO}$  optical depth correction method,  $N_{\text{H}_2}^{13}$ , respectively), mean  $^{13}\text{CO}(1-0)$  optical depth ( $\tau^{13}$ ), mean CO excitation temperature ( $T$ ) and mass calculated via the X-factor method,  $M^{12}$ , and the  $^{13}\text{CO}$  optical depth correction method,  $M^{13}$ , are displayed.

Arm <sup>a</sup>	Region	$v_{\text{LSR}}$	$\Delta v_{\text{FWHM}}$	$N_{\text{H}_2}^{12}$	$N_{\text{H}_2}^{13}$	$\tau^{13}$	$T$	$M^X$	$M^{13}$
			[ $\text{km s}^{-1}$ ]		[ $10^{21} \text{cm}^{-2}$ ]		[K]	[ $M_{\odot}$ ]	
Sag.	SNR <sup>b</sup>	-	-	0.5 - 1.5 <sup>c</sup>	-	-	-	1700-5000	-
Scutum	SNR <sup>b</sup>	-	-	0.3 - 1.0 <sup>c</sup>	-	-	-	19300-22000	-
-Crux	-40A <sup>d</sup>	-39.60±0.10	2.5±0.2	2.4 - 7.2	1.9 - 5.6	0.06	8	590-1700	100-300
(near)	-40B <sup>d</sup>	-38.97±0.03	1.2±0.1	2.2 - 6.4	3.4 - 10	0.2	10	220-670	120-370
	-40C <sup>d</sup>	-36.73±0.06	2.8±0.2	2.2 - 6.7	3.7 - 11	0.1	8	2200-6800	690-2000
	-40D <sup>d</sup>	-42.49±0.03	2.2±0.1	3.0 - 9.0	3.3 - 9.6	0.1	9	1100-3300	460-1400
	-50A <sup>e</sup>	-47.32±0.04	3.5±0.1	4.1 - 12	6.4 - 19	0.1	16	3400-10000	1800-5200
	-50B <sup>e</sup>	-47.18±0.02	2.0±0.1	2.0 - 5.9	2.0 - 5.9	0.2	9	1100-3200	520-1500
	-50C <sup>e</sup>	-49.70±0.10	3.4±0.1	2.8 - 8.4	6.4 - 19	0.1	12	6300-19000	2000-5900
Norma	SNR <sup>b</sup>	-	-	1.2 - 3.5 <sup>c</sup>	-	-	-	140000-420000	-
-Cygnus									

<sup>a</sup> Most likely Galactic Arm association with reference to Figure 5. Distances used to derive masses were 1.2, 3.5 and 7.2 kpc for the Sagittarius, Scutum-Crux and Norma-Cygnus arms, respectively. <sup>b</sup> Elliptical region of HESS J1534–571 identified at 843 MHz, see Figure 1. <sup>c</sup> Average values within the region. <sup>d</sup> See Figure 2. <sup>e</sup> See Figure 3.

molecular gas has an arc-like morphological distribution consisting of a north-south aligned chain of at least five clumps and a westward extension to the northern edge of the chain comprised of at least three clumps. Minimal diffuse extended CO(1-0) emission is observed across the central and south-east HESS J1534–571 field.

The molecular mass in the  $-44$  to  $-35 \text{ km s}^{-1}$  velocity-range is separated from the Scutum-Crux arm in velocity-space, as indicated as “-40B/C” in Figure 5a. Along the adjacent Galactic arm, between  $-54$  and  $-45 \text{ km s}^{-1}$ , a clump of mass  $\sim 10^3 M_{\odot}$  is coincident with the west of HESS J1534–571, while clouds of mass  $\sim 10^3 M_{\odot}$  and  $\sim 10^4 M_{\odot}$  lie to the east and south, respectively. On average within each region, all Scutum-Crux Arm molecular gas components are observed to have  $^{13}\text{CO}(1-0)$  optical depth and CO excitation temperature within common ranges of 0.06 to 0.2 and 8 to 16 K, respectively.

Prompted by the existence of the distinct arc-like clumpy molecular structure, which is offset in velocity-space from the main arm, we examined atomic H I emission from the Scutum-Crux arm for indications of an association with HESS J1534–571. In Section 4.1, we discuss a candidate association for HESS J1534–571.

We note that a complete infrared bubble at  $[l, b] = [324.06, -0.81]$  (S8, Churchwell et al. 2006) is coincident with region -40A to the north-east of HESS J1534–571, suggesting a connection between high-mass OB star formation and the  $10^2$  to  $10^3 M_{\odot}$  clump. Alternatively, the Norma-Cygnus arm gas is also a potential association for the infrared bubble, particularly given the nearby broad and ring-like clump features in that region (see Figure 3). It is unclear if this feature has any connection to the gamma-ray emission originating from the region.

### 3.5 The Norma-Cygnus Arm

CO(1-0)-traced molecular gas between  $-85$  and  $-56 \text{ km s}^{-1}$  is associated with the Norma-Cygnus Arm. The proximity to the tangent point makes precise distance determinations for this arm difficult (see Figure 5d). Assuming a distance of 7.2 kpc, CO traces a total molecular mass of  $1.4$  to  $4.2 \times 10^5 M_{\odot}$  towards HESS J1534–571. In Figure 3, this arm is divided into three velocity slices to highlight individual spectral features (images of Figure 4 in rows labelled ‘Norma-Cygnus Arm’).

Broad, spatially-extended CO/ $^{13}\text{CO}(1-0)$  emission features are coincident with the north-east of HESS J1534–571, and a circular structure is centred on  $[l, b] = [324.05, -0.90]$  in the narrow  $-62.5$  to  $-56 \text{ km s}^{-1}$  velocity-range. Gas connected to these features extend towards the centre of the SNR, and gas from the north extends southwards coincident with the northern half of the western TeV gamma-ray emission. Gas connected to this feature extends in velocity-space across  $20 \text{ km}^{-1}$ , and can be seen in all three CO images of the Norma-Cygnus arm in Figure 3. This, and the ring-like structure may indicate turbulence related to star formation.

## 4 DISCUSSION

Towards the SNR HESS J1534–571, Mopra CO(1-0) emission traces molecular gas from 5 Galactic arms. At least three of these have a molecular gas morphology which displays overlap with gamma-ray emission from the TeV gamma-ray shell. Such features offer the potential to explore possible hadronic components of gamma-ray emission in HESS J1534–571.

In Sections 3.2 to 3.5 CO(1-0)-traced molecular gas of the Sagittarius, Scutum-Crux and Norma-Cygnus arms has been described. Gas-gamma-ray overlap may make these arms candidates for association with HESS J1534–571.



In the case of the Scutum-Crux arm gas the molecular and atomic structure are suggestive of a wind-blown bubble candidate for HESS J1534–571. In Section 4.1 and 4.3 we explore this scenario.

We emphasise that the spectral line gas data presented in our study cannot be employed to explore scenarios where HESS J1534–571 is not associated with gas. We investigate the potential of an association with gas that may take the form of a cavity blown out by a progenitor star (e.g. Fukui et al. 2003; Fukuda et al. 2014; Fukui et al. 2017), or overlap between gas clouds and gamma-ray emission (e.g. Aharonian et al. 2008; Nicholas et al. 2011; Abdalla et al. 2016) which might suggest a hadronic scenario where CRs diffuse into nearby molecular gas. A perfect correlation between gas and gamma-rays is not necessary in the latter case, because hadronic gamma-ray emission will not only be proportional to the gas proton density, but the density of CRs. This is not expected to be uniform.

#### 4.1 A Scutum-Crux Arm Gas Association for HESS J1534-571

The discovery of clumpy molecular structures in Section 3.4 prompted a re-examination of SGPS HI data at nearby velocities (see Appendix A). Figure 6 (top) highlights a dip in HI emission at  $\sim 47.5 \text{ km s}^{-1}$ , consistent with the Scutum-Crux arm at a distance of  $\sim 3.5 \text{ kpc}$ . A HI gradient surrounds the SNR from the south-east to the north, then west. Abdalla et al. (2018) considered this dip as one of the two example potential ISM associations when discussing the energetics of HESS J1534–571. To the south of HESS J1534–571, where HI emission is less pronounced, a  $\sim 10^3$  to  $10^4 M_\odot$  molecular cloud (“–50C”, see Figure 3 and Table 1) is present, as traced by CO(1-0).

The HI dip may correspond to a bubble in atomic gas blown-out by the progenitor of HESS J1534–571. In such a scenario analogous to that of SNR Vela Jr (Fukui et al. 2017; Maxted et al. 2018b) or RX J1713.7–3946 (e.g. Inoue et al. 2012), nearby dense molecular clumps have sparse atomic outer layers stripped by strong stellar winds, leaving dense clumps within a wind-blown bubble. Following the supernova explosion, the ejecta expands into the void and interacts with the progenitor termination shock and stripped clumps.

An association between HESS J1534–571 and Scutum-Crux arm gas would suggest that the SNR was the product of a core-collapse (CC) event at a kinematic distance of  $\sim 3.5 \text{ kpc}$ . The implied TeV luminosity of HESS J1534–571 at this distance is comparable to SNRs RX J1713.7–3946, RX J0852.0–4622, and HESS J1731–347 (see Table 2).

#### 4.2 X-rays from HESS J1534-571

Signatures of an interaction might be detectable at X-ray energies. Dense molecular clumps embedded within young ( $\sim 10^3 \text{ yr}$ ) SNR shells are sometimes associated with X-ray nodes caused by high energy electrons emitting non-thermally in magnetic fields on the boundary of dense gas. For example, X-ray emission peaks have been linked to shock compression regions near dense molecular gas in the young SNR RX J1713.7–3946 (e.g. Cassam-Chenaï et al. 2004;

Acero et al. 2009; Sano et al. 2010; Inoue et al. 2012; Maxted et al. 2013), while thermal X-ray emission from plasma becomes prominent as SNRs approach the radiative phase of evolution, sometimes directly adjacent to molecular clouds (e.g. see Nakamura et al. 2014).

In Figure 6 (bottom), we show Suzaku X-ray emission regions from Saji et al. (2018) overlaid on the HESS J1534–571 gas association candidate. Some of these regions encompass several peaks in X-ray emission. Four 6.4 keV Fe line emission regions and nine soft X-ray emission regions were detected, labelled SFe1-4 (‘Saji Fe’) and SsX1-9 (‘Saji soft X-rays’), respectively, in Figure 6. X-ray emission in the northwest (SFe4, SsX9) and south (SsX3, SsX5 and SsX9) appear to lie on the boundary of molecular clumps, suggesting that these originate from SNR shock-molecular cloud interactions with gas identified in this study. The strongest Fe emission detection, which is in the east of the remnant, SFe1, appears at the boundary of a large  $3.4$  to  $10 \times 10^3 M_\odot$  molecular cloud (region –50A), also suggestive of an association. However, no potential gas associations can be identified for X-ray emission regions SFe3, SFe2, SsX4, SsX5 and SsX8, while the coverage of the Suzaku maps do not include the southwest region of HESS J1534–571, where  $\sim 3$  to  $10 \times 10^3 M_\odot$  of molecular gas lies. It follows that we have no firm conclusions on X-ray associations of HESS J1534–571, and we leave further studies of this as future work.

#### 4.3 HESS J1534-571 Distance Constraints from Radio Brightness

In this section we investigate the HESS J1534–571 distance through a comparison with models fitted to a sample of well-studied SNRs.

Pavlovic et al. (2014) compiled a  $\Sigma - D$  calibrating sample of 65 Galactic SNRs with reliable distances, 1 GHz flux measurements and angular diameters (required to calculate  $\Sigma$  and  $D$ ). The orthogonal fit to this data was then used as a calibrator to estimate the distance to SNRs with unreliable (or no) distance estimates. Vukotić et al. (2014) then argued that a more robust calibration could be achieved with estimates of the data probability density function (PDF) in the  $\log \Sigma - \log D$  plane instead of using the standard procedures based on fitted trend lines. This method was further statistically improved in Bozzetto et al. (2017), where the data were smoothed using a 2-D Gaussian to generate a probability density function (PDF). The kernel widths were obtained by minimizing the Bootstrap Integrated Mean Square Error (i.e. BIMSE, for a detailed procedure description see Bozzetto et al. 2017). The PDF was calculated on a  $100 \times 100$  grid for the plotted variables (linear diameter and 1 GHz radio continuum surface brightness, both expressed on logarithmic scales) using 100 bootstrap resamplings to yield a BIMSE value for each set of examined kernel bandwidths. The set of bandwidths with the smallest BIMSE value (0.16 in  $\log D$  and 0.56 in  $\log \Sigma$ ) was used for smoothing.

In order to use the  $\Sigma - D$  relation from Pavlovic et al. (2014), we scaled the MOST 843 MHz flux measurements of HESS J1534–571 to 1 GHz assuming a simple scaling law  $S \propto \nu^\alpha$  where the spectral index is  $-0.5$ . We note that a change of 20% in the assumed spectral index results in a change in the 1 GHz flux smaller than the resolution of the calculated PDF, thus errors from the extrapolation are con-

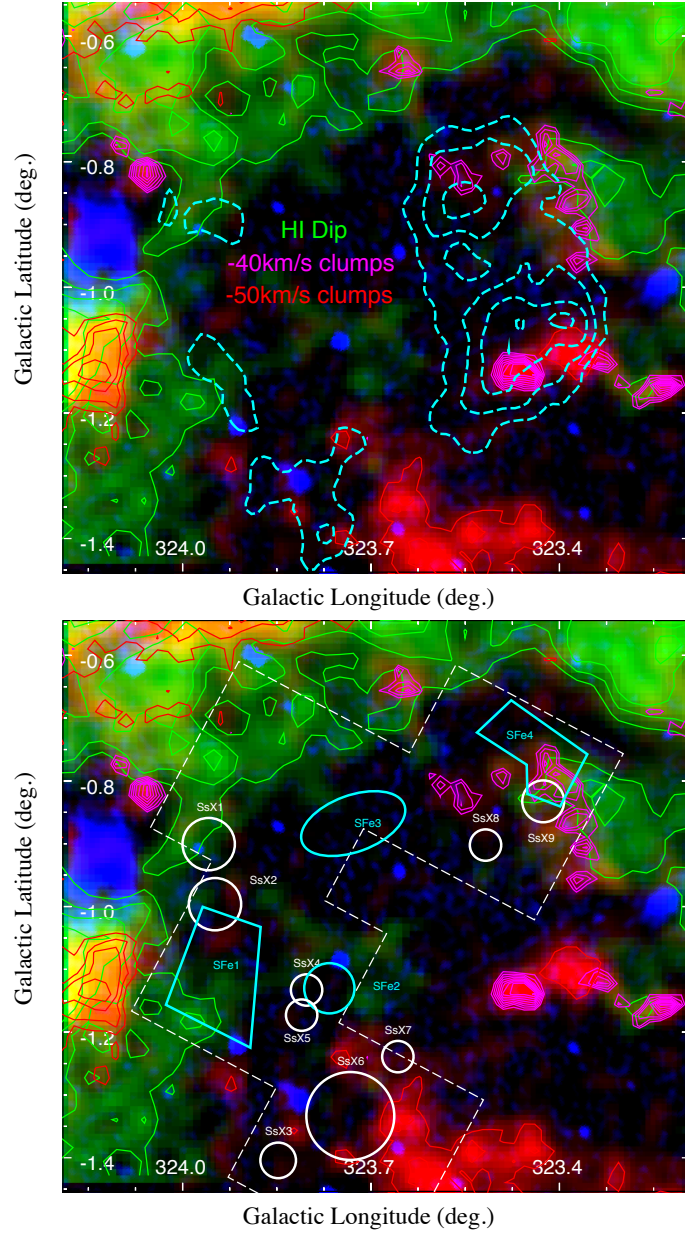


**Figure 6.** SGPS H I emission integrated from  $-50$  to  $-45$   $\text{km s}^{-1}$  (green), Mopra CO(1-0) emission integrated from  $-54$  to  $-45$   $\text{km s}^{-1}$  (red) and from  $-45$  to  $-35$   $\text{km s}^{-1}$  (magenta contours) and MOST 843 MHz continuum emission (blue). In the top image, HESS TeV gamma-ray significance (cyan contours) are overlaid. In the bottom image, X-ray emission regions from Saji et al. (2018) are overlaid (see Section 4.1 for details). The dashed-white region indicates Suzaku X-ray observation coverage, cyan regions indicate 6.4 keV Fe emission line regions and white circles indicate soft X-ray emission regions.

sidered negligible in our investigation. The MOST telescope recorded a HESS J1534–571 843 MHz flux of 0.49 Jy, but this value excludes emission from structures at scales larger than 25 arcminutes (Green et al. 2014). Following Abdalla et al. (2018), we thus assume 0.49 Jy to be a lower limit. Double this value is assumed to be an appropriate upper limit, because most of the radio flux from SNRs generally originates from the forward and reverse shocks, which are likely narrower than 25 arcminutes in the case of HESS J1534–571.

In Figure 7, we display the PDF of the 1 GHz radio continuum flux as a function of SNR diameter. The flux range of HESS J1534–571 is indicated in this graph by 2 horizon-

tal lines, and the probability distribution as a function of diameter along these 2 lines of constant surface brightness are displayed in Figure 8. The presented probability distributions are calculated by normalizing from bidimensional data in Figure 7 at the specified values.

For the purpose of distance estimates (independent of any suggested gas association in this paper), we use median values of distributions in Figure 8. For the purpose of error estimates, we use a 75% confidence interval by integrating to lower and higher values starting from the median value. The integration is performed in an asymmetrical manner such that one side is integrated until the PDF value on that side

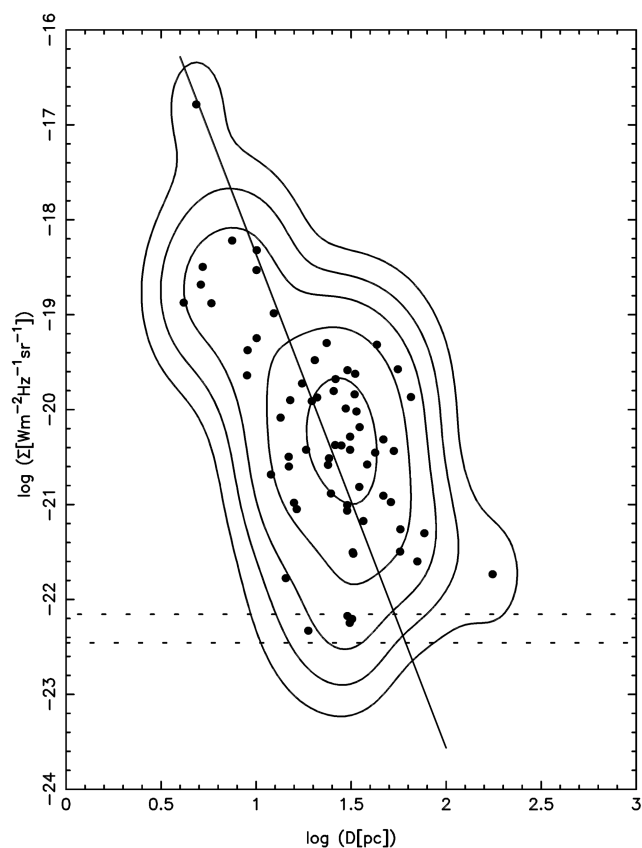


**Figure 7.** The Probability Density Function of the 1 GHz radio flux of 65 SNRs (from Pavlović et al. 2014). The contour levels are at 0.02, 0.05, 0.1, 0.2 and 0.4. The solid line is the best fit from Pavlović et al. while the dashed lines are the 1 GHz flux bounds ( $\Sigma$ ) extrapolated from the HESS J1534–571 MOST 843 MHz flux (Green et al. 2014).

falls below the PDF value on the other side (for a more detailed description on error estimation algorithms in one dimensional PDFs see Vukotić et al. 2014).

The orthogonal fit calibration from Pavlović et al. (2014) (see Figure 7),  $\log \Sigma = -13.16 - 5.2 \log D$ , yields a HESS J1534–571 distance of 4.8 kpc and 4.2 kpc with fractional error  $\sim 50\%$ , for lower and upper flux limits, respectively.<sup>4</sup>

Our median-based estimate from Figure 8 suggests a distance of 2.5 kpc with a 1.0 to 4.6 kpc confidence (75%) interval and 2.6 kpc with a 1.0 to 5.7 kpc confidence interval, for the lower and upper flux values, respectively. These ranges cover smaller distances than those implied by the orthogonal offset method (Figure 7, 4.2 to 4.8 kpc  $\pm 50\%$ ), but both methods imply distances consistent with the near Scutum-Crux Arm gas (3.5 kpc, see Section 4.1). This is in

<sup>4</sup> We note that the sample of SNRs used for the orthogonal fit line is biased towards smaller diameters and larger radio continuum fluxes due to the sensitivity limits of radio continuum SNR searches, so the uncertainty may be larger.

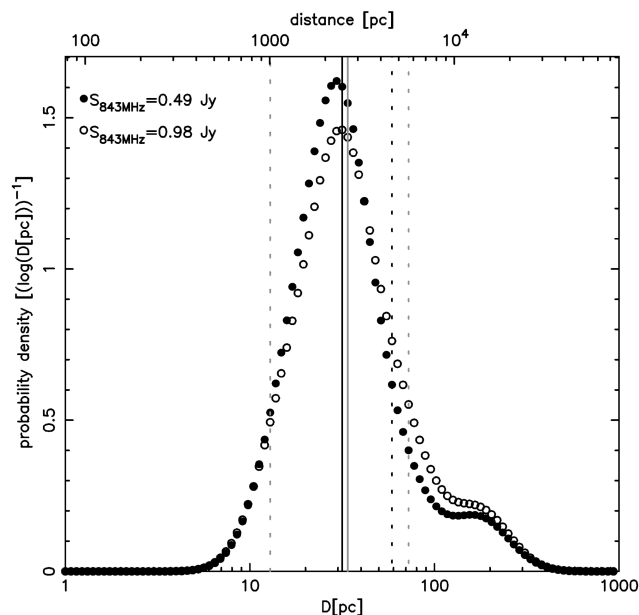


**Figure 8.** The diameter probability density distributions derived from the PDF bidimensional distribution for the upper and lower HESS J1534–571 843 MHz flux values from Figure 7 (open and closed circles, respectively) scaled to 1 GHz assuming a spectral index of  $-0.5$ . The median values of the lower and upper flux-limit distributions are indicated by the solid and grey lines, respectively. Dashed vertical lines represent the 75% confidence intervals of the two diameter distributions. The lower confidence interval (dashed grey) of the two diameter distributions is the same for both cases, while the upper confidence intervals of the two cases are represented by the black (0.49 Jy case) and grey (0.98 Jy case) dashed lines.

contrast to the Sagittarius and Norma-Cygnus arms at  $\sim 1.2$  and  $\sim 7.2$  kpc, respectively.

We further note that our method generally yields lower distances than those implied by simple  $\Sigma$ -offset methods (see Pavlović et al. 2013; Pavlović et al. 2014). The robust nature of the PDF-based method is likely to give a better insight into the confidence level of the estimates, which can also be very helpful when comparing with estimates from other (independent) methods - in this case possible CO associations.

In the case of HESS J1534–571, Abdalla et al. (2018) also recognised that a  $\Sigma$ -offset distance ( $\sim 15$ – $20$  kpc) was flawed and suggested a distance closer to  $\sim 5$  kpc based on the assumption of under-luminous radio emission, similar to RX J1713.7–3946. Our calculation validates this suggestion and is consistent with the 3.5 kpc distance suggested by the candidate Scutum-Crux Arm gas association with HESS J1534–571 and previous studies ( $\sim 4$  to 5 kpc and  $\sim 6 \pm 2$  kpc, Araya 2017; Saji et al. 2018, respectively).

#### 4.4 The Age of HESS J1534–571

In Section 4.1, we noted a plausible association of SNR HESS J1534–571 with the Scutum-Crux Galactic arm at a distance of  $\sim 3.5$  kpc. In this section, we discuss the age of the SNR using both a simple parametrisation that assumes sim-



ilarities with RX J1713.7–3946 and a more detailed model with varied initial inputs.

A SNR age that mirrors the evolution of known TeV shells can be approximated by scaling known TeV shell-type SNR ages according to the Sedov relation,

$$t \sim \left( \frac{R_{\text{sh}}}{R_{\text{calib}}} \right)^{5/2} t_{\text{calib}} \quad (4)$$

where  $R_{\text{sh}}$  and  $R_{\text{calib}}$  are the shock radii of the SNR under scrutiny (in this case HESS J1534–571) and the SNR used as a calibrator, respectively.  $t_{\text{calib}}$  is the age of the SNR used as a calibrator. Implicit assumptions include both SNRs being in the Sedov phase, evolving in homogeneous media of the same density and an equivalent initial explosion energy.

After 1600 years of evolution, SNR RX J1713.7–3946 reached a diameter of  $\sim 20$  pc (e.g. Wang et al. 1997; Fukui et al. 2003)<sup>5</sup>, with a proportion of the SNR evolution time taking place within a wind-blown bubble. We use these values in Equation 4 to approximate a HESS J1534–571 age in the case that HESS J1534–571 results from similar initial conditions to RX J1713.7–3946. This yields ages of 1.1, 15 and 89 kyr for assumed distances of 1.2, 3.5 and 7.2 kpc, respectively.

A second method estimated the HESS J1534–571 age using SNR evolution modeling software by Leahy & Williams (2017), which primarily utilises the approach outlined in Truelove & McKee (1999). This software models the forward and reverse shock radii and velocity, and keV X-ray emission of SNRs as a function of SNR age. We considered three candidate distances (1.2, 3.5 and 7.2 kpc). Model scenarios for both the 3.5 kpc distance and the 1.2 kpc distance were assumed to be low-explosion energy ( $0.5 \times 10^{51}$  erg) events due to low HESS J1534–571 radio luminosity. The 7.2 kpc distance model was assumed to have a moderate initial energy of  $10^{51}$  erg. A homogeneous ISM density between  $0.01$  and  $1.0 \text{ cm}^{-3}$  was assumed in order to derive conservative age lower and upper limits, respectively, except in the case of the 3.5 kpc distance model where we assume  $0.01$ – $0.1 \text{ cm}^{-3}$ . This is motivated by the existence of the suggested gas association for HESS J1534–571 (see Figure 6, Section 4.1). All models were assumed to have an ejecta mass of  $2 M_{\odot}$ .

Our age solution for HESS J1534–571 derived via Leahy & Williams modeling are displayed in Table 2. For comparison, published age and distance constraints for other shell-type SNRs with shell-like gamma-ray morphology (RX J0852.0–4622, RX J1713.7–3946 and HESS J1731–347) are also included in Table 2.

For the H I dip distance of 3.5 kpc, the HESS J1534–571 would be in the Sedov phase of evolution with a corresponding age of 8 to 24 kyr. The predicted forward shock velocity and electron temperatures are 400 to  $1200 \text{ km s}^{-1}$  and  $\text{kT} \sim 0.2$  to 1 keV, respectively. Based on a plasma temperature derived from soft X-rays by Saji et al. (2018),  $\text{kT} = 1.1^{+0.5}_{-0.3}$  keV, modelling possibly favours the ages nearer to 8 kyr than 24 kyr assuming that the X-ray detection primarily originates from electrons in the forward shock. The

range of derived ages encompasses that estimated by scaling an RX J1713.7–3946-like explosion (12 kyr, Equation 4).

#### 4.5 Future Studies

In previous SNR studies, the identification of X-ray peaks adjacent to dense clumps have been noted to signal a gas-shock interaction (e.g. Cassam-Chenaï et al. 2004), while the comparison of spectral-line-derived column densities with X-ray absorption column density measurements (e.g. Maxted et al. 2018a) have constrained SNR distance. In this context, further X-ray emission observations that achieve full spatial-coverage of HESS J1534–571 will be a key step to understanding the distance, age and nature of HESS J1534–571, particularly towards regions –40D and –50B, which currently lack coverage at keV energies. Furthermore, additional X-ray coverage will aid in a search for an associated CCO, which could constrain the SNR distance and age with modeling of thermal emission.

Furthermore, in the bright TeV core-collapse SNRs RX J1713.7–3946, HESS J1731–347 and RX J0852.0–4622, gamma-ray features may hint at the existence of CR acceleration through spatial gas/gamma-ray correspondence within the TeV shell (Moriguchi et al. 2005; Fukuda et al. 2014; Fukui et al. 2017, respectively), CR interactions in nearby gas (e.g. potentially Cui et al. 2016; Capasso et al. 2017; Maxted et al. 2018a), or spectral flattening resulting from energy-dependent hadron diffusion into dense molecular cores (Gabici et al. 2009; Zirakashvili & Aharonian 2010; Inoue et al. 2012; Fukui et al. 2012; Maxted et al. 2012; Gabici & Aharonian 2014). The  $\sim 10$ -fold sensitivity-increase and arcminute-scale resolution of the next generation of gamma-ray instrument, Cherenkov Telescope Array (CTA, Acero et al. 2017), will allow CR acceleration in young SNRs to be probed by searching for these gas/gamma-ray signatures. In the case of HESS J1534–571, sub-arcminute Mopra CO/<sup>13</sup>CO(1-0) maps will enable investigations of features in high resolution gamma-ray maps to help distinguish between hadronic and leptonic emission scenarios.

## 5 CONCLUSIONS

We present Mopra Southern Galactic Plane CO and <sup>13</sup>CO(1-0) emission maps towards the TeV gamma-ray supernova remnant HESS J1534–571 (G323.). We examine the morphology of molecular cloud structures in five Galactic arms, and highlight Scutum-Crux arm molecular cores that are at a consistent velocity with a H I dip. We suggest this to be associated with a progenitor wind-blown cavity of a HESS J1534–571 core-collapse event. The distance corresponding to the cavity,  $\sim 3.5$  kpc, is consistent with our two independent analyses of the radio continuum brightness ( $\sim 4.5 \pm 2.5$  kpc and  $\sim 2.5^{+3.0}_{-1.5}$  kpc) and recently-published distance estimates from leptonic gamma-ray emission modelling and X-ray absorption calculations ( $\sim 4$  to 5 kpc and  $\sim 6 \pm 2$  kpc, respectively). Based on the assumption of a 3.5 kpc distance solution, we suggest the SNR to be in the Sedov-Taylor phase of evolution with an age of 8 to 24 kyr.

<sup>5</sup> We note that some controversy around the 1600 yr age solution for RX J1713.7–3946 exists, but these can be rectified if the RX J1713.7–3946 explosion was optically sub-luminous (see Fesen et al. 2012)



**Table 2.** The diameter ( $D$ ), age, coincident molecular mass, and 1 to 10 TeV spectral index ( $\Gamma_\gamma$ ) and luminosity ( $L_{\gamma,1-10\text{TeV}}$ ) (with reference to Abdalla et al. 2018) of core-collapse TeV supernova remnants with constrained distances ( $d$ ). Where multiple possible distance solutions exist, each distance is considered.

SNR	$d^a$ (kpc)	$D^a$ (pc)	Age <sup>a</sup> (yr)	Molecular Mass <sup>a</sup> ( $M_\odot$ )	$\Gamma_\gamma$	$L_{\gamma,1-10\text{TeV}}$ ( $10^{33}\text{ erg s}^{-1}$ )
RX J0852.0–4622	0.75	26	$\sim 10^3$	$\sim 1 \times 10^3$	1.81	5.7
RX J1713.7–3946	1.0	20	$1.6 \times 10^3$	$9 \times 10^3$	2.06	7.2
HESS J1731–347	3.2	30	$\sim 2.5 \times 10^3$	$5 \times 10^4$	2.32	8.5
	5.2	49	"	$4\text{--}5 \times 10^4$		22.4
HESS J1534–571	1.2	17	$^{b,e} 1.3\text{--}5.5 \times 10^3$	$1.7\text{--}5.0 \times 10^3$	2.51	1.1
	3.5	49	$^{c,e} 8\text{--}24 \times 10^3$	$0.9\text{--}2.2 \times 10^4$		9.6
	7.2	100	$^{d,e} > 32 \times 10^3$	$1.4\text{--}4.2 \times 10^5$		40.4

<sup>a</sup> Gas associations, age and distance constraints: (RX J0852.0–4622: Katsuda et al. 2008; Allen et al. 2015; Fukui et al. 2017), (RX J1713.7–3946: Wang et al. 1997; Fukui et al. 2003; Moriguchi et al. 2005; Aharonian et al. 2007; Fukui et al. 2012), (HESS J1731–347: Tian et al. 2008; Fukuda et al. 2014; Cui et al. 2016; Maxted et al. 2018a)

<sup>b</sup> Assuming an initial explosion energy of  $0.5 \times 10^{51}$  erg and constant H density of  $0.01\text{--}1.0\text{ cm}^{-3}$ . <sup>c</sup> Assuming an initial explosion energy of  $0.5 \times 10^{51}$  erg and constant H density of  $0.01\text{--}0.1\text{ cm}^{-3}$ . <sup>d</sup> Assuming an initial explosion energy of  $1.0 \times 10^{51}$  erg and constant H density of  $> 0.01\text{ cm}^{-3}$ . <sup>e</sup> See Section 4.3 for further details.

## ACKNOWLEDGMENTS

The Mopra Telescope is part of the Australia Telescope and is funded by the Commonwealth of Australia for operation as a National Facility managed by the CSIRO. The University of New South Wales Mopra Spectrometer Digital Filter Bank used for these Mopra observations was provided with support from the Australian Research Council, together with the University of New South Wales, the University of Adelaide, University of Sydney, Monash University and the CSIRO. We thank the Australian Research Council for helping to fund this work through a Linkage Infrastructure, Equipment and Facilities (LIEF) grant (LE16010094). D. Urosevic, B. Vukotic and M. Z. Pavlovic acknowledge support by the project No. 176005, “Emission nebulae: structure and evolution,” supported by the Ministry of Education, Science, and Technological Development of the Republic of Serbia. We thank Shigetaka Saji for providing us with Suzaku X-ray emission coordinates promptly following our request.

## REFERENCES

- Abdalla H., et al., 2016, preprint, ([arXiv:1609.00600](https://arxiv.org/abs/1609.00600))  
 Abdalla H., et al., 2018, preprint, ([arXiv:1801.06020](https://arxiv.org/abs/1801.06020))  
 Acero F., Ballet J., Decourchelle A., Lemoine-Goumard M., Ortega M., Giacani E., Dubner G., Cassam-Chenaï G., 2009, *A&A*, **505**, 157  
 Acero F., Lemoine-Goumard M., Renaud M., Ballet J., Hewitt J. W., Rousseau R., Tanaka T., 2015, *A&A*, **580**, A74  
 Acero F., et al., 2017, *ApJ*, **840**, 74  
 Ackermann M., et al., 2013, *Science*, **339**, 807  
 Aharonian F., et al., 2007, *A&A*, **464**, 235  
 Aharonian F., et al., 2008, *A&A*, **481**, 401  
 Allen G. E., Chow K., DeLaney T., Filipović M. D., Houck J. C., Pannuti T. G., Stage M. D., 2015, *ApJ*, **798**, 82  
 Araya M., 2017, *ApJ*, **843**, 12  
 Bachiller R., Cernicharo J., 1986, *A&A*, **166**, 283  
 Bell A. R., 1978, *MNRAS*, **182**, 147  
 Bolatto A. D., Wolfire M., Leroy A. K., 2013, *ARA&A*, **51**, 207  
 Bozzetto L. M., et al., 2017, *ApJS*, **230**, 2  
 Braiding C., et al., 2015, *Publ. Astron. Soc. Australia*, **32**, e020  
 Braiding C., Wong G. F., Maxted N., Burton M. G., Blackwell R., 2018, *Publ. Astron. Soc. Australia*  
 Burton M. G., et al., 2013, *Publ. Astron. Soc. Australia*, **30**, e044  
 Capasso M., et al., 2017, *AIP Conference Proceedings*, **1792**, 040026  
 Cassam-Chenaï G., Decourchelle A., Ballet J., Sauvageot J.-L., Dubner G., Giacani E., 2004, *A&A*, **427**, 199  
 Cernicharo J., Bachiller R., 1984, *A&AS*, **58**, 327  
 Churchwell E., et al., 2006, *The Astrophysical Journal*, **649**, 759  
 Cui Y., Pühlhofer G., Santangelo A., 2016, *A&A*, **591**, A68  
 Dame T. M., Hartmann D., Thaddeus P., 2001, *ApJ*, **547**, 792  
 Fesen R. A., Kremer R., Patnaude D., Milisavljevic D., 2012, *AJ*, **143**, 27  
 Frail D. A., Goss W. M., Reynoso E. M., Giacani E. B., Green A. J., Otrupcek R., 1996, *AJ*, **111**, 1651  
 Frerking M. A., Langer W. D., Wilson R. W., 1982, *ApJ*, **262**, 590  
 Fukuda T., Yoshiike S., Sano H., Torii K., Yamamoto H., Acero F., Fukui Y., 2014, *ApJ*, **788**, 94  
 Fukui Y., et al., 2003, *PASJ*, **55**, L61  
 Fukui Y., et al., 2012, *ApJ*, **746**, 82  
 Fukui Y., et al., 2017, *ApJ*, **850**, 71  
 Gabici S., Aharonian F. A., 2014, *MNRAS*, **445**, L70  
 Gabici S., Aharonian F. A., Casanova S., 2009, *MNRAS*, **396**, 1629  
 Green A. J., Reeves S. N., Murphy T., 2014, *PASA*, **31**, e042  
 Inoue T., Yamazaki R., Inutsuka S.-i., Fukui Y., 2012, *ApJ*, **744**, 71  
 Katsuda S., Tsunemi H., Mori K., 2008, *ApJ*, **678**, L35  
 Kostić P., Vukotić B., Urošević D., Arbutina B., Prodanović T., 2016, *MNRAS*, **461**, 1421  
 Ladd N., Purcell C., Wong T., Robertson S., 2005, *Publ. Astron. Soc. Australia*, **22**, 62  
 Lang K. R., 1980, *Astrophysical Formulae. A Compendium for the Physicist and Astrophysicist.*  
 Leahy D. A., Williams J. E., 2017, *AJ*, **153**, 239  
 Maxted N., et al., 2012, *MNRAS*, **422**, 2230  
 Maxted N., et al., 2013, *Publ. Astron. Soc. Australia*, **30**, e055  
 Maxted N., et al., 2018a, *MNRAS*, **474**, 662  
 Maxted N., et al., 2018b, *AJ*, submitted, 000

- McClure-Griffiths N. M., Dickey J. M., Gaensler B. M., Green A. J., Haverkorn M., Strasser S., 2005, *ApJS*, **158**, 178
- Moriguchi Y., Tamura K., Tawara Y., Sasago H., Yamaoka K., Onishi T., Fukui Y., 2005, *ApJ*, **631**, 947
- Nakamura R., et al., 2014, *PASJ*, **66**, 62
- Nicholas B., Rowell G., Burton M. G., Walsh A., Fukui Y., Kawamura A., Longmore S., Keto E., 2011, *MNRAS*, **411**, 1367
- Nicholas B. P., Rowell G., Burton M. G., Walsh A. J., Fukui Y., Kawamura A., Maxted N. I., 2012, *MNRAS*, **419**, 251
- Okamoto R., Yamamoto H., Tachihara K., Hayakawa T., Hayashi K., Fukui Y., 2017, *ApJ*, **838**, 132
- Pavlović M. Z., Urošević D., Vukotić B., Arbutina B., Göker Ü. D., 2013, *ApJS*, **204**, 4
- Pavlovic M. Z., Dobardzic A., Vukotic B., Urosevic D., 2014, *Serbian Astronomical Journal*, **189**, 25
- Pavlović M. Z., Urošević D., Arbutina B., Orlando S., Maxted N., Filipović M. D., 2018, *ApJ*, **852**, 84
- Puehlhofer G., Eger P., Sasaki M., Gottschall D., Capasso M., H. E. S. S. Collaboration 2016, in *XMM-Newton: The Next Decade*. p. 61
- Saji S., Matsumoto H., Nobukawa M., Nobukawa K. K., Uchiyama H., Yamauchi S., Koyama K., 2018, *PASJ*,
- Sano H., et al., 2010, *ApJ*, **724**, 59
- Sault R. J., Teuben P. J., Wright M. C. H., 1995, in Shaw R. A., Payne H. E., Hayes J. J. E., eds, *Astronomical Society of the Pacific Conference Series Vol. 77, Astronomical Data Analysis Software and Systems IV*. p. 433 ([arXiv:astro-ph/0612759](https://arxiv.org/abs/astro-ph/0612759))
- Tian W. W., Leahy D. A., Haverkorn M., Jiang B., 2008, *ApJ*, **679**, L85
- Truelove J. K., McKee C. F., 1999, *ApJS*, **120**, 299
- Vallée J. P., 2016, *AJ*, **151**, 55
- Vukotić B., Jurković M., Urošević D., Arbutina B., 2014, *MNRAS*, **440**, 2026
- Wang Z. R., Qu Q.-Y., Chen Y., 1997, *AAP*, **318**, L59
- Wilson T. L., Rohlfs K., Hüttemeister S., 2013, *Tools of Radio Astronomy*. Springer, [doi:10.1007/978-3-642-39950-3](https://doi.org/10.1007/978-3-642-39950-3)
- Zirakashvili V. N., Aharonian F. A., 2010, *ApJ*, **708**, 965

## APPENDIX A: HI INVESTIGATION

We examined SGPS H I (McClure-Griffiths et al. 2005) emission towards the supernova remnant, HESS J1534–571. H I emission was integrated in  $5\text{km s}^{-1}$  velocity slices in a search for H I dip features that align with the MOST 843 MHz radio emission of HESS J1534–571, while colour scales were adjusted to highlight H I emission gradients. A H I dip identified in this study is highlighted in Figure 6.

This paper has been typeset from a  $\text{T}_{\text{E}}\text{X}/\text{L}^{\text{A}}\text{T}_{\text{E}}\text{X}$  file prepared by the author.

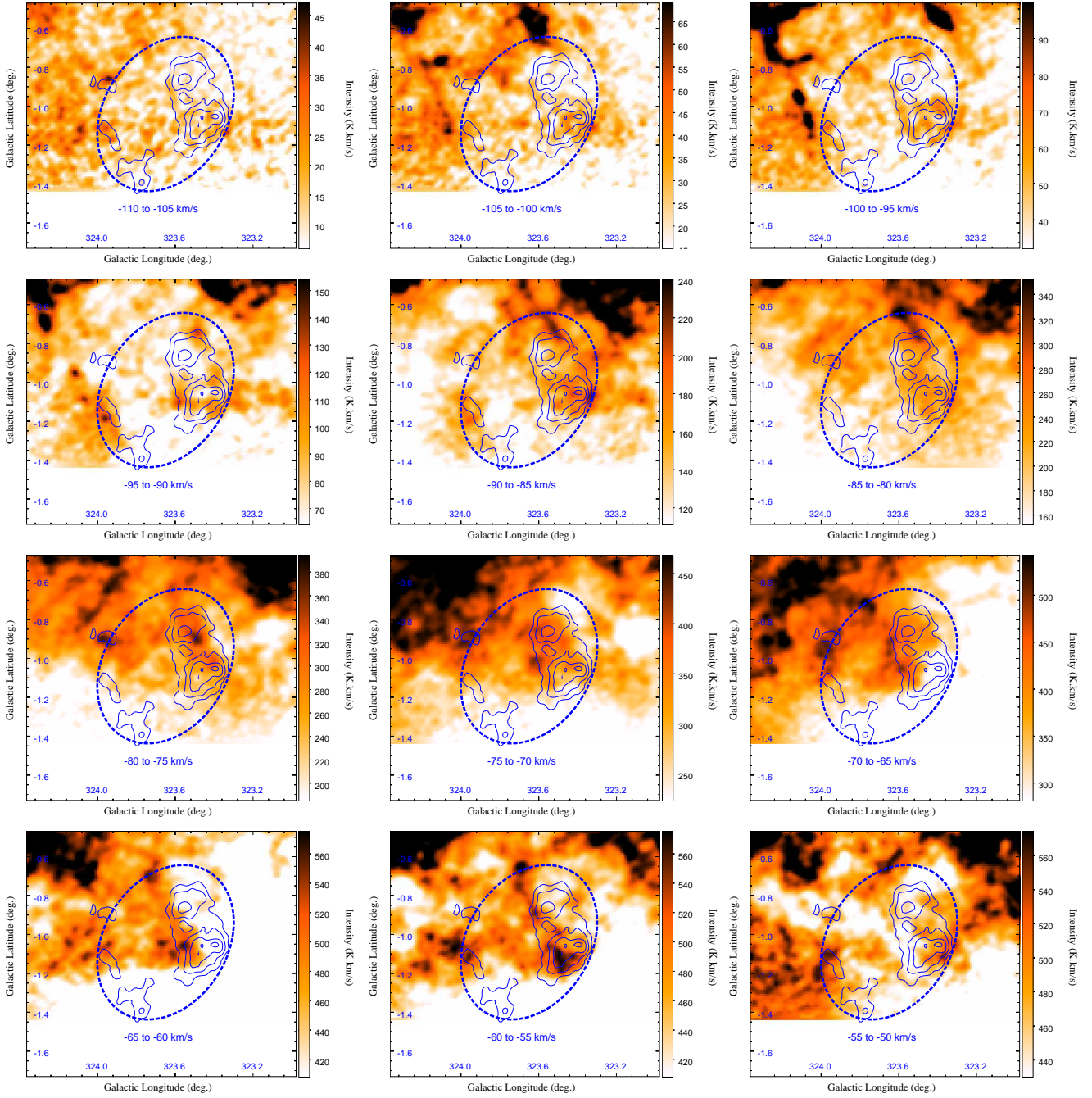


**Figure A1.** HI emission integrated in 5 km/s velocity slices. 3, 4, 5 and 6 $\sigma$  TeV gamma-ray emission contours of the associated source HESS J1534–571 are overlaid. A blue dashed ellipse indicates the characterisation of the 843 MHz emission, which has a centre of  $[\alpha, \delta] = [05:34:30.1-57:12:03]$  and axes diameter of  $51 \times 38'$ .



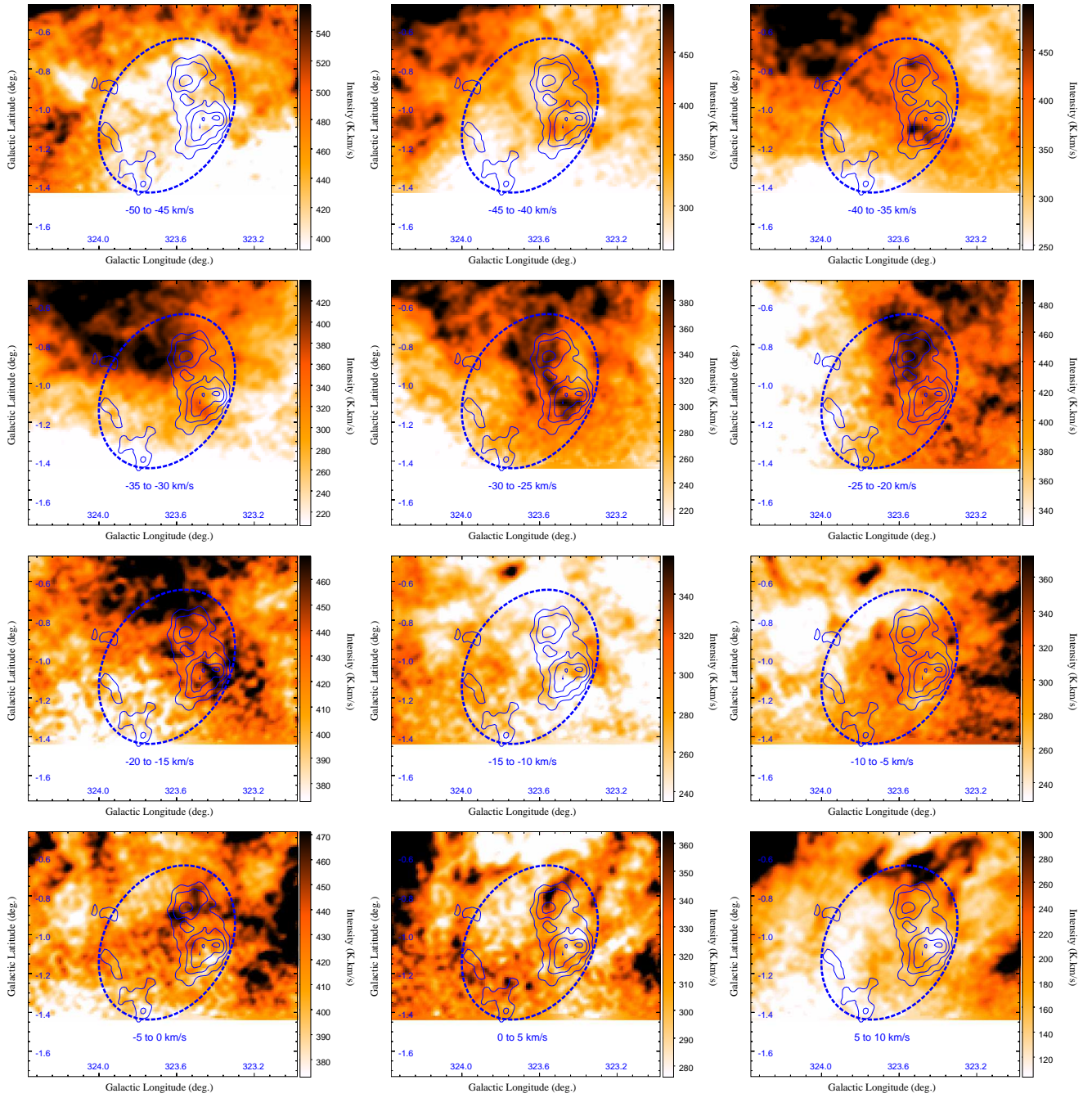


Figure A2. Same as Figure A1, but for different velocity-integration ranges.